

Fast evaluation of far-field signals for time-domain wave propagation

Scott E. Field and Stephen R. Lau

the date of receipt and acceptance should be inserted later

Abstract Time-domain simulation of wave phenomena on a finite computational domain often requires a fictitious outer boundary. An important practical issue is the specification of appropriate boundary conditions on this boundary, often conditions of complete transparency. Attention to this issue has been paid elsewhere, and here we consider a different, although related, issue: far-field signal recovery. Namely, from smooth data recorded on the outer boundary we wish to recover the far-field signal which would reach arbitrarily large distances. These signals encode information about interior scatterers and often correspond to actual measurements. This article expresses far-field signal recovery in terms of time-domain convolutions, each between a solution multipole moment recorded at the boundary and a sum-of-exponentials kernel. Each exponential corresponds to a pole term in the Laplace transform of the kernel, a finite sum of simple poles. Greengard, Hagstrom, and Jiang have derived the large- ℓ (spherical-harmonic index) asymptotic expansion for the pole residues, and their analysis shows that, when expressed in terms of the exact sum-of-exponentials, large- ℓ signal recovery is plagued by cancellation errors. Nevertheless, through an alternative integral representation of the kernel and its subsequent approximation by a *smaller* number of exponential terms (kernel compression), we are able to alleviate these errors and achieve accurate signal recovery. We empirically examine scaling relations between the parameters which determine a compressed kernel, and perform numerical tests of signal "teleportation" from one radial value r_1 to another r_2 , including the case $r_2 = \infty$. We conclude with a brief discussion on application to other hyperbolic equations posed on non-flat geometries where waves undergo backscatter.

1 Introduction

This article describes sphere-to-sphere propagation of smooth data for the ordinary 3-space dimensional wave equation [1, 2, 3, 4]. As an application, consider evolving the wave equation (4) on a finite computational domain with a spherical outer boundary of radius r_1 , recording as a time-series the solution restricted to the boundary sphere, and –as a post-processing step– recovering what the solution reaching $r_2 > r_1$ would be. In this application neither the computational domain nor the final time need be extended. For many applications, the post-processing step would be faster than evolving the wave equation on a commensurately larger spacetime domain, whilst avoiding accumulation of phase or other errors typical of long-time integrations. We shall refer to the propagation of solution data from radius r_1 to radius

Scott E. Field
Department of Physics, Joint Space Science Institute,
and Maryland Center for Fundamental Physics
University of Maryland
College Park, MD 20742, USA

Center for Radiophysics and Space Research,
Cornell University,
Ithaca, New York 14853, USA

Stephen R. Lau
Department of Mathematics and Statistics
University of New Mexico
Albuquerque, NM 87131, USA

r_2 as *teleportation*, and in the limit $r_2 \rightarrow \infty$ as *asymptotic-waveform evaluation*. As discussed in the concluding section, our methods likely extend to a certain class of hyperbolic equations.

To further elucidate the idea, consider evolution of the simple 1-space dimensional wave equation,

$$-\partial_t^2 \Psi + \partial_x^2 \Psi = 0, \quad (1)$$

on $x_0 \leq x \leq x_1$, subject to Sommerfeld boundary conditions and with compactly supported initial data. The general solution of d'Alembert is

$$\Psi(t, x) = F(x - t) + G(x + t), \quad (2)$$

where the "outgoing" wave is $F(x - t)$. As follows from the assumption of compact support and (2), the wave value passing x_1 at time t will reach $x_2 > x_1$ at time $t + (x_2 - x_1)$, and

$$\Psi(t + (x_2 - x_1), x_2) = F(x_1 - t) = \Psi(t, x_1). \quad (3)$$

This formula constitutes the simplest possible teleportation scheme, only accounting for the time-delay between the spacetime points (t_1, x_1) and (t_2, x_2) .

Turn now to the 3-space dimensional wave equation,

$$(-\partial_t^2 + \partial_x^2 + \partial_y^2 + \partial_z^2)\psi = S(t, x, y, z), \quad (4)$$

subject to initial data and source S of compact support. We imagine a region of space enclosed by a spherical outer boundary of radius r_1 which need not be large. This boundary sphere is also called the *extraction sphere*, and beyond it there are no scatters and both the initial data and source term vanish. Furthermore, on the boundary sphere we place exact radiation outer boundary conditions [6,5].¹ Let the Cartesian coordinates $\mathbf{x} = (x, y, z)$ be expressed as $\mathbf{x} = r\boldsymbol{\theta}$, with $\boldsymbol{\theta} = (\sin \theta \cos \phi, \sin \theta \sin \phi, \cos \theta)$ the direction cosines associated to spherical polar coordinates.² From the extraction-sphere data $r_1 \psi(t, r_1 \boldsymbol{\theta})$ we seek to recover the signal $r_2 \psi(t + (r_2 - r_1), r_2 \boldsymbol{\theta})$ which would reach arbitrarily large distances r_2 (the extra radial factors account for the $1/r$ fall-off of ψ).

We adopt the following approach to far-field signal recovery: (i) derive an exact $r_1 \rightarrow r_2$ procedure/relationship in the spherical-harmonic-Laplace transform domain ("frequency domain"), and then (ii) approximate this exact relationship in a way which allows for a simple inversion of the Laplace transform [3]. Owing to the spatial spherical harmonic transform, the approach remains nonlocal in space. For the wave equation (4), the relationship in the frequency domain (whether exact or approximate) involves a sum of simple poles; whence the corresponding time-domain procedure involves a history-dependent convolution based on a sum-of-exponentials kernel. For a given spherical-harmonic polar index ℓ , the *exact* sum-of-exponentials kernel involves precisely ℓ terms. As recently shown by Greengard, Hagstrom, and Jiang [4] and described further below, direct evaluation of the *exact* sum-of-poles frequency domain kernel is problematic for large ℓ . Indeed, in this case the complex residues in the sum vary in modulus over many orders of magnitude, and the sum is plagued by cancellation errors. Ref. [4] has also described a method for evaluating the *time-domain* kernel via stable recursion relations, assuming that the pole locations (Bessel-MacDonald zeros) have been precomputed.

Using the technique of *kernel compression* [6,7,8,9], this paper considers approximation of the exact frequency domain kernel. Our approximations are based on an integral expression for the frequency-domain kernel (cf. Eq. (42)) which affords well-conditioned evaluation of the exact frequency domain kernel at imaginary Laplace frequencies, but by itself is not useful for the time-domain. With expression (42) and a given integer $d \ll \ell$, we may construct an accurate rational approximation of the exact kernel which is itself a sum of d simple poles, and therefore also determines a sum-of-exponentials kernel in the time-domain (now with fewer terms). While offering no analytical proof, we empirically demonstrate that kernel evaluation based on the d -term approximate expansion is more accurate than evaluation based on the ℓ -term exact expansion. Moreover, we examine scaling relations between the parameters which determine a compressed kernel. Our approach was recently developed in Ref. [3] for cases where closed-form kernel expressions were unavailable, and the concluding section remarks on applicability of the technique beyond the ordinary wave equation case. We also give a more detailed derivation of Greengard, Hagstrom, and Jiang's large- ℓ asymptotic result [4] for the exact kernel residues.

¹ An efficient simultaneous implementation of teleportation and radiation boundary conditions (RBC) would rely on common pole locations for both the teleportation and RBC kernels, thereby using the same ODEs for both recovery of the teleported signal and enforcement of the RBC. Reference [3] noted that, when achievable, the resulting teleportation kernels were of reduced accuracy. However, the preliminary study made in Ref. [3] involved kernels for blackhole perturbations, and future work should explore the issue for the wave equation.

² Here with the convention that θ is the polar and ϕ the azimuthal angle.

2 Teleportation kernels

This section reviews the origin and structure of teleportation kernels [1, 2, 3, 4], mostly following the presentation from [3]. In the Laplace frequency s -domain, each such kernel is a finite sum of simple poles in the complex s -plane. Assembling various results from [10, 11] and Abramowitz and Stegun's compendium [12] (hereafter AS), this section also considers the residues of a teleportation kernel, in particular deriving a large- ℓ asymptotic expansion. Our analysis in section 2.3 is an elaboration of results given in Ref. [4].

2.1 Derivation

Assuming that $S = 0$ (the source plays no direct role in what follows), we start by expanding the solutions to Eq. (4) as

$$\psi(t, x, y, z) = \frac{1}{r} \sum_{\ell=0}^{\infty} \sum_{m=-\ell}^{\ell} \Psi_{\ell m}(t, r) Y_{\ell m}(\theta, \phi), \quad (5)$$

where the $Y_{\ell m}(\theta, \phi)$ are standard spherical harmonics, i.e. the eigenfunctions of the Laplace-Beltrami operator on the unit sphere. Substitution of (5) into (4) determines that for each (ℓ, m) pair the time-domain *multipole* $\Psi_{\ell m}(t, r)$ obeys the *radial wave equation*,

$$\partial_t^2 \Psi_{\ell m} - \partial_r^2 \Psi_{\ell m} + \frac{\ell(\ell+1)}{r^2} \Psi_{\ell m} = 0. \quad (6)$$

Introducing the Laplace transform,

$$\widehat{\Psi}_{\ell m}(s, r) = \int_0^{\infty} e^{-st} \Psi_{\ell m}(t, r) dt, \quad (7)$$

we transform Eq. (6), with the result

$$\left[s^2 - \frac{d^2}{dr^2} + \frac{\ell(\ell+1)}{r^2} \right] \widehat{\Psi}_{\ell m} = s \Psi_{\ell m}(0, r) + \Psi_{\ell m}'(0, r). \quad (8)$$

Solution of this equation by the method of variation of parameters requires solutions to the homogeneous equation; these can be expressed in terms of modified Bessel functions.

Consider initial data of compact support, chosen to vanish outside of $r = r_1 - \delta$, with $0 < \delta \ll 1$. Then for $r \geq r_1$, the general solution to (8) is the *outgoing* one

$$\widehat{\Psi}_{\ell m}^{\text{out}}(s, r) = A_{\ell m}(s) s^{\ell} e^{-sr} W_{\ell}(sr), \quad W_{\ell}(z) = \sum_{k=0}^{\ell} \frac{c_{\ell k}}{z^k}, \quad c_{\ell k} = \frac{1}{2^k k!} \frac{(\ell+k)!}{(\ell-k)!}, \quad (9)$$

where $z = sr$, $A_{\ell m}(s)$ is independent of r , and (cf. AS **10.1.9** and **10.2.15**)

$$W_{\ell}(z) = \sqrt{\frac{2z}{\pi}} e^z K_{\ell+1/2}(z). \quad (10)$$

Here $K_{\nu}(z)$ is a modified spherical Bessel function (MacDonald's function) of Bessel order $\nu \equiv \ell + 1/2$ [13, 12]; ν has this meaning throughout.

The structure of the Laplace-domain solution (9) determines the following algebraic relationship between solution values:

$$e^{s(r_2-r_1)} \widehat{\Psi}_{\ell m}^{\text{out}}(s, r_2) = \widehat{\Phi}_{\ell}(s, r_1, r_2) \widehat{\Psi}_{\ell m}^{\text{out}}(s, r_1) + \widehat{\Psi}_{\ell m}^{\text{out}}(s, r_1), \quad (11)$$

where we have defined the frequency-domain teleportation kernel (cf. Eq. (31) of [3])

$$\widehat{\Phi}_{\ell}(s, r_1, r_2) = -1 + \frac{W_{\ell}(sr_2)}{W_{\ell}(sr_1)}. \quad (12)$$

Here the "minus 1" factor ensures that $\widehat{\Phi}_\ell(s, r_1, r_2)$ decays for large s , and therefore has an inverse Laplace transform which is a classical function. Intuitively, the "minus 1" factor also isolates $\widehat{\Phi}_\ell(s, r_1, r_2)\widehat{\Psi}_{\ell m}^{\text{out}}(s, r_1)$ as the piece of the propagating wave which is altered as it moves from r_1 to r_2 . Indeed, when $\ell = 0$ the kernel is zero and (11) becomes

$$e^{s(r_2-r_1)}\widehat{\Psi}_{00}^{\text{out}}(s, r_2) = \widehat{\Psi}_{00}^{\text{out}}(s, r_1). \quad (13)$$

This formula involves only the wave transit time, and could have been obtained directly in the time-domain (see the introduction). From Eq. (12) the asymptotic signal for any ℓ is determined by

$$\widehat{\Phi}_\ell(s, r_1, \infty) = \frac{1 - W_\ell(sr_1)}{W_\ell(sr_1)}, \quad (14)$$

where we have used $W_\ell(\infty) = 1$. The kernel $\widehat{\Phi}_\ell(s, r_1, r_2)$ teleports a signal $\widehat{\Psi}_{\ell m}^{\text{out}}(s, r_1)$ of frequency s from an extraction sphere of radius r_1 to $r_2 \leq \infty$. Expression (11) can be implemented in frequency-domain solvers. We now turn to the time-domain case.

The next subsection shows that (12) can be represented as a sum of simple poles,

$$\widehat{\Phi}_\ell(s, r_1, r_2) = \sum_{j=1}^{\ell} \frac{a_{\ell j}(r_1, r_2)}{s - b_{\ell j}/r_1}. \quad (15)$$

Therefore, by well-known properties of the Laplace transform, the inverse transformation of Eq. (11) is (dropping the "out" superscript)

$$\Psi_{\ell m}(t + (r_2 - r_1), r_2) = \int_0^t \Phi_\ell(t - t', r_1, r_2) \Psi_{\ell m}(t', r_1) dt' + \Psi_{\ell m}(t, r_1), \quad (16)$$

where the time-domain teleportation kernel is a sum of exponentials,

$$\Phi_\ell(t, r_1, r_2) = \sum_{k=1}^{\ell} a_{\ell k}(r_1, r_2) e^{b_{\ell k} t / r_1}. \quad (17)$$

The formulas (15,17) express signal teleportation as a time-domain convolution, and for low- ℓ they are numerically useful. However, as shown in [4] and reviewed below, for high ℓ they become exponentially ill-conditioned. Section 3.2 discusses *kernel compression*, which involves approximation of (17) by a sum³

$$\Phi_\ell(t, r_1, r_2) \simeq \Xi_\ell(t, r_1, r_2) = \sum_{k=1}^d \gamma_{\ell k}(r_1, r_2) e^{\beta_{\ell k}(r_1, r_2)t} \quad (18)$$

of $d \leq \ell$ exponentials. Below we demonstrate empirically that compression also alleviates the large- ℓ catastrophic cancellation due to the exponential variation in size (31) of the residues.

A convolution based on either (17) or (18) can be directly implemented in time-domain solvers, or carried out as a post-processing step. The time series $\Psi_{\ell m}(t, r_1)$ must be generated by a numerical solver, whereas the teleportation technique allows for reduction of the computational domain. That is, the signal $\Psi_{\ell m}(t + (r_2 - r_1), r_2)$ that would reach r_2 is written explicitly in terms of data recorded on the extraction sphere. Appendix A provides an error estimate for the teleportation of noisy numerical data. Efficiency gains in computing $r_2\psi(t, r_2\theta)$ by way of signal teleportation, as opposed to direct numerical simulation, will depend on choices for r_1 , r_2 , the final simulation time, and the number of (ℓ, m) multipoles required to accurately resolve $r_1\psi(t, r_1\theta)$ with a truncated expansion (5). These considerations are further discussed in Refs. [3,4].

³ Ref. [3] used Ξ_ℓ^E , $\gamma_{\ell k}^E$, and $\beta_{\ell k}^E$ for these quantities, where E stands for "evaluation". In [3] the same symbols *without* E superscripts were used for similar quantities associated with radiation boundary conditions.

2.2 Kernel residues

In terms of the Bessel-MacDonald zeros $\{b_{\ell j} : j = 1, \dots, \ell\}$ the function $W_\ell(z)$ has the form

$$W_\ell(z) = z^{-\ell} \prod_{j=1}^{\ell} (z - b_{\ell j}), \quad (19)$$

which follows from (10) and shows that the roots of $W_\ell(z)$ are the same as those of $K_{\ell+1/2}(z)$. The treatise by Watson shows that all $b_{\ell j}$ lie in the left-half plane $\{z : \text{Re} z < 0\}$. Moreover, for even ℓ these roots come in $\ell/2$ conjugate pairs, while for odd ℓ we have $(\ell - 1)/2$ conjugate pairs and precisely one negative real root. In terms of the Bessel order ν the scaled roots $b_{\ell k}/\nu$ are known to accumulate on a fixed transcendental curve in the left-half plane; see Fig. 1.

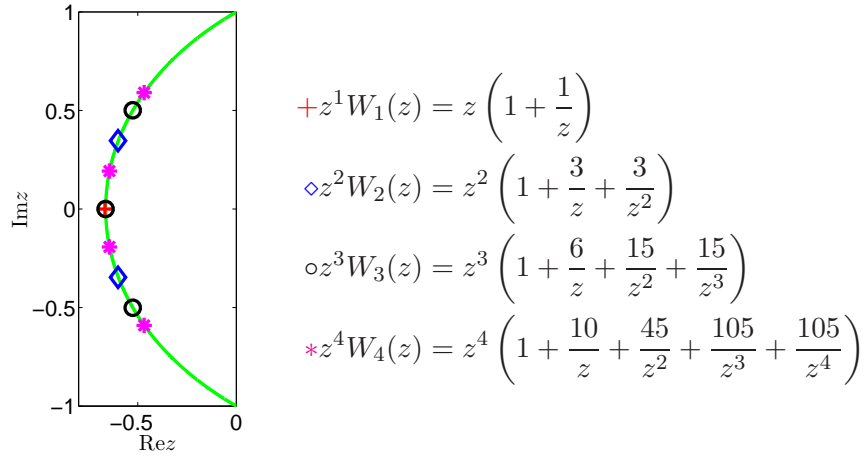


Fig. 1 The left figure displays scaled zeros of $z^\ell W_\ell(z)$ which, through Eq. (15), are related to the scaled zeros of the teleportation kernel. Here we plot the scaled zeros $(\ell + 1/2)^{-1} b_{\ell, k}$ for $1 \leq \ell \leq 4$ whose Bessel polynomial is shown in the right figure. In the limit $\ell + 1/2 \rightarrow \infty$ these zeros accumulate on the transcendental curve (green). Evidently the agreement holds even for the lowest ℓ , at least to the eye.

From Eqs. (12,19) the kernel can be written as

$$\hat{\Phi}_\ell(s, r_1, r_2) = -1 + \frac{\prod_{j=1}^{\ell} (s - b_{\ell j}/r_2)}{\prod_{j=1}^{\ell} (s - b_{\ell j}/r_1)} = \sum_{j=1}^{\ell} \frac{a_{\ell j}(r_1, r_2)}{s - b_{\ell j}/r_1}. \quad (20)$$

Since the poles are simple, we compute the residues as ⁴

$$a_{\ell j}(r_1, r_2) = \lim_{s \rightarrow b_{\ell j}/r_1} (s - b_{\ell j}/r_1) \hat{\Phi}_\ell(s, r_1, r_2) = r_1^{\ell-1} \frac{\prod_{k=1}^{\ell} (b_{\ell j}/r_1 - b_{\ell k}/r_2)}{\prod_{k=1, k \neq j}^{\ell} (b_{\ell j} - b_{\ell k})}. \quad (21)$$

The last expression in (21) implies that $a_{\ell j}(r_1, r_2) = r_1^{-1} a_{\ell j}(1, r_2/r_1)$, from which we infer the scaling relation

$$\hat{\Phi}_\ell(s, r_1, r_2) = \hat{\Phi}_\ell(sr_1, 1, r_2/r_1). \quad (22)$$

To facilitate further analysis of the residues, start with

$$a_{\ell j}(r_1, r_2) = \frac{W_\ell(b_{\ell j} r_2/r_1)}{r_1 W'_\ell(b_{\ell j})}, \quad (23)$$

⁴ The residues $a_{\ell j}(1, r)$ are precisely those considered in [4].

a formula which agrees with (21). We now write $a_{\ell j}(r_1, r_2)$ in terms of standard special functions, starting with MacDonald's function. From (10), we get

$$W_\ell(b_{\ell j}r_2/r_1) = \sqrt{\frac{2b_{\ell j}}{\pi} \frac{r_2}{r_1}} e^{b_{\ell j}r_2/r_1} K_{\ell+1/2}(b_{\ell j}r_2/r_1) \quad (24a)$$

$$W'_\ell(b_{\ell j}) = \sqrt{\frac{2b_{\ell j}}{\pi}} e^{b_{\ell j}} K'_{\ell+1/2}(b_{\ell j}). \quad (24b)$$

Note that $K_{\ell+1/2}(z)$ is defined only on the slit plane (due to the branch associated with the square root factor). Therefore, for odd ℓ the purely real root $b_{\ell, 1+(\ell-1)/2}$ is not in the domain of analyticity. Nevertheless, with appropriate cancellation of square-root factors, the following expression is valid even for this root

$$a_{\ell j}(r_1, r_2) = \frac{1}{r_1} \sqrt{\frac{r_2}{r_1}} e^{(r_2/r_1-1)b_{\ell j}} \frac{K_{\ell+1/2}(b_{\ell j}r_2/r_1)}{K'_{\ell+1/2}(b_{\ell j})}. \quad (25)$$

To use Olver's uniform asymptotic formulas for Bessel functions of large order and argument (see in particular AS 9.3.37 and 9.3.45), we need to express (25) in terms of the first Hankel function. To this end, we start with the first equation in AS 10.2.15 (which involves the first spherical Hankel function defined in AS 10.1.16):

$$\sqrt{\frac{\pi}{2z}} K_{\ell+1/2}(z) = \frac{i\pi}{2} e^{i(\ell+1)\pi/2} h_\ell^{(1)}(ze^{i\pi/2}), \quad -\pi < \arg z \leq \frac{1}{2}\pi. \quad (26)$$

Next, using the relationship between spherical and cylindrical Hankel functions given in AS 10.1.1, we get

$$\sqrt{\frac{\pi}{2z}} K_{\ell+1/2}(z) = \frac{i\pi}{2} e^{i(2\ell+1)\pi/4} \sqrt{\frac{\pi}{2z}} H_{\ell+1/2}^{(1)}(ze^{i\pi/2}), \quad -\pi < \arg z \leq \frac{1}{2}\pi. \quad (27)$$

There are two branch cuts associated with the right-hand expression. The first is the usual cut along the negative real axis (in the z -plane) associated with the square root. The second results from the branch associated with $H_{\ell+1/2}^{(1)}(\bullet)$; due to the rotated argument this cut is the positive imaginary axis (in the z -plane). Across both cuts the right-hand expression in (27) jumps by a sign, whereas, due to (26) and the domain of analyticity for $h_\ell^{(1)}(\bullet)$, the left-hand expression in (27) is analytic on the origin-punctured z -plane. Therefore, we work with the expression

$$K_{\ell+1/2}(z) = \epsilon \frac{i\pi}{2} e^{i(2\ell+1)\pi/4} H_{\ell+1/2}^{(1)}(iz), \quad (28)$$

where $\epsilon = -1$ in the second quadrant and $\epsilon = 1$ otherwise. Using this result, we cast (25) into the form

$$a_{\ell j}(r_1, r_2) = -\frac{i}{r_1} \sqrt{\frac{r_2}{r_1}} e^{(r_2/r_1-1)b_{\ell j}} \frac{H_{\ell+1/2}^{(1)}(ib_{\ell j}r_2/r_1)}{H_{\ell+1/2}^{(1)'}(ib_{\ell j})}. \quad (29)$$

Now introduce the scaled zeros $\tilde{b}_{\ell j} = (\ell + 1/2)^{-1} b_{\ell j}$. In terms of these

$$a_{\ell j}(r_1, r_2) = -\frac{i}{r_1} \sqrt{\frac{r_2}{r_1}} e^{(r_2/r_1-1)\nu \tilde{b}_{\ell j}} \frac{H_\nu^{(1)}(i\nu \tilde{b}_{\ell j}r_2/r_1)}{H_\nu^{(1)'}(i\nu \tilde{b}_{\ell j})}, \quad (30)$$

where derivative in the denominator can be eliminated with the identity $2H_\nu^{(1)'}(z) = H_{\nu-1}^{(1)}(z) - H_{\nu+1}^{(1)}(z)$. The last two expressions agree with [4] when $r_2 = r$ and $r_1 = 1$.

2.3 Asymptotics

Following Greengard, Hagstrom, and Jiang [4], we now use (30) in tandem with AS 9.3.37 and 9.3.45 to derive an asymptotic formula for $a_{\ell j}(r_1, r_2)$. Since the time domain kernel (17) is real valued, the roots and residues come in conjugate pairs. Whence it suffices to consider only those scaled roots $\tilde{b}_{\ell j}$ obeying $-\pi \leq \arg \tilde{b}_{\ell j} < -\frac{1}{2}\pi$. The result is

$$a_{\ell j}(r_1, r_2) \sim \frac{i\tilde{b}_{\ell j}}{2r_1} \left(\frac{r_2}{\pi r_1} \right)^{1/2} (1 + \tilde{b}_{\ell j}^2)^{-1/4} (1 + \tilde{b}_{\ell j}^2 (r_2/r_1)^2)^{-1/4} \frac{e^{\nu\psi_{\ell j}(r_1, r_2)}}{(a_j)^{-1/4} \text{Ai}'(a_j)}, \quad \ell \rightarrow \infty. \quad (31)$$

In this expression

$$\psi_{\ell j}(r_1, r_2) = (r_2/r_1 - 1)\tilde{b}_{\ell j} - \log \frac{1 + \sqrt{1 + \tilde{b}_{\ell j}^2 (r_2/r_1)^2}}{i\tilde{b}_{\ell j} r_2/r_1} + \sqrt{1 + \tilde{b}_{\ell j}^2 (r_2/r_1)^2}, \quad (32)$$

and a_j is the j th root of the Airy function $\text{Ai}(y)$. To achieve the correct correspondence between the $\tilde{b}_{\ell j}$ and the a_j , formula (31) assumes that the set $\{\tilde{b}_{\ell j} : j = 1, \dots, \ell\}$ is ordered from the bottom of the third quadrant upwards, i.e. for $\ell = 3$ the (unscaled) roots b_{3j} are ordered as follows (of these we consider only b_{31} and b_{32}).

$$\begin{aligned} b_{31} &= -1.8389\text{e}+00 - 1.7544\text{e}+00i \\ b_{32} &= -2.3222\text{e}+00 + 0.0000\text{e}+00i \\ b_{33} &= -1.8389\text{e}+00 + 1.7544\text{e}+00i \end{aligned}$$

Remark 1 At the expense of introducing a second expansion with its own error, (31) may be further reduced through the following large- j formulae (see the appendix of [11]):

$$a_j \sim -(\frac{3}{2}\pi)^{2/3}(j - \frac{1}{4})^{2/3}, \quad \text{Ai}'(a_j) \sim \frac{(-1)^{j-1}}{\sqrt{\pi}}(\frac{3}{2}\pi)^{1/6}(j - \frac{1}{4})^{1/6}, \quad (a_j)^{-1/4} \text{Ai}'(a_j) \sim \frac{(-1)^{j-1}}{\sqrt{\pi}}e^{-i\pi/4}. \quad (33)$$

We now turn to the derivation of (31). Since we consider those $i\tilde{b}_{\ell j}$ in the fourth quadrant, the arguments of the Hankel functions in (30) are certainly in the sector of validity for the following expansions (AS 9.3.37 and 9.3.45):

$$H_\nu^{(1)}(\nu w) \sim 2e^{-i\pi/3}\nu^{-1/3} \left(\frac{4\zeta}{1-w^2} \right)^{1/4} \text{Ai}(e^{2\pi i/3}\nu^{2/3}\zeta) \quad (34a)$$

$$H_\nu^{(1)'}(\nu w) \sim \frac{4}{w}e^{4i\pi/3}\nu^{-2/3} \left(\frac{1-w^2}{4\zeta} \right)^{1/4} \text{Ai}'(e^{2\pi i/3}\nu^{2/3}\zeta), \quad (34b)$$

which hold for $|\arg w| \leq \pi - \epsilon$. In these expansions (see AS 9.3.38, but note that the z and \ln in AS are our w and \log)

$$\frac{2}{3}\zeta^{3/2} = \log \frac{1 + \sqrt{1-w^2}}{w} - \sqrt{1-w^2}, \quad (35)$$

defines ζ implicitly as function of w .

We first consider evaluation of (34b) with $w = i\tilde{b}_{\ell j}$. As $\nu \rightarrow \infty$ the scaled roots $\tilde{b}_{\ell j}$ obey [10]

$$i\tilde{b}_{\ell j} \sim w(\zeta_j) + O(\nu^{-1}), \quad \zeta_j = e^{-2\pi i/3}\nu^{-2/3}a_j, \quad (36)$$

uniformly in j . Therefore, the desired expression for (34b) is

$$H_\nu^{(1)'}(\nu i\tilde{b}_{\ell j}) \sim -2\sqrt{2}\nu^{-1/2}(\tilde{b}_{\ell j})^{-1}(1 + \tilde{b}_{\ell j}^2)^{1/4}(a_j)^{-1/4}\text{Ai}'(a_j). \quad (37)$$

In canceling terms to reach this expression, we have paid due attention to the branch associated with the fourth root.

Next, we turn to (34a) with $w = i\tilde{b}_{\ell j}r_2/r_1$,

$$H_\nu^{(1)}(\nu i\tilde{b}_{\ell j}r_2/r_1) \sim 2e^{-i\pi/3}\nu^{-1/3} \left(\frac{4\zeta_r}{1 + \tilde{b}_{\ell j}^2 (r_2/r_1)^2} \right)^{1/4} \text{Ai}(e^{2\pi i/3}\nu^{2/3}\zeta_r), \quad (38)$$

where $\zeta_r = \zeta(ib_{\ell j}r_2/r_1)$, that is ζ_r stems from (35) with $w = ib_{\ell j}r_2/r_1$. The analysis given in [11] (pages 355-356) shows that $\frac{1}{3}\pi < \arg(\zeta_r) < \pi$, provided w is in fourth quadrant. The large argument asymptotics $\text{Ai}(y) \sim \frac{1}{2}\pi^{-1/2}y^{-1/4}e^{-\frac{2}{3}y^{3/2}}$ of the Airy function determine that

$$\text{Ai}(e^{2\pi i/3}\nu^{2/3}\zeta) \sim \frac{1}{2}\pi^{-1/2}\nu^{-1/6}e^{\pi i/3}\zeta^{-1/4}e^{-\frac{2}{3}\nu\zeta^{3/2}}. \quad (39)$$

To reach this equation from the Airy expansion, we have assumed $\frac{1}{3}\pi < \arg \zeta < \pi$ and $-\pi < \arg(e^{2\pi i/3}\zeta) < -\frac{1}{3}\pi$. Recall that ζ_r obeys these inequalities. With the last result and further consideration of the fourth-root branch, we get

$$H_\nu^{(1)}(\nu ib_{\ell j}r_2/r_1) \sim \sqrt{2}\pi^{-1/2}\nu^{-1/2}\left(1 + \tilde{b}_{\ell j}^2(r_2/r_1)^2\right)^{-1/4}e^{-\frac{2}{3}\nu\zeta_r^{3/2}}, \quad (40)$$

and finally

$$\frac{H_\nu^{(1)}(\nu ib_{\ell j}r_2/r_1)}{H_\nu^{(1)'}(\nu i\tilde{b}_{\ell j})} \sim -\frac{\tilde{b}_{\ell j}}{2\sqrt{\pi}}\left(1 + \tilde{b}_{\ell j}^2\right)^{-1/4}\left(1 + \tilde{b}_{\ell j}^2(r_2/r_1)^2\right)^{-1/4}\frac{e^{-\frac{2}{3}\nu\zeta_r^{3/2}}}{(a_j)^{-1/4}\text{Ai}'(a_j)}. \quad (41)$$

This equation and (30) yield (31).

3 Numerical approximation of teleportation kernels

This section treats the numerical approximation of frequency-domain teleportation kernels $\hat{\Phi}_\ell(s, r_1, r_2)$. Construction of our approximations requires that we are able to accurately evaluate $\hat{\Phi}_\ell(iy, r_1, r_2)$ for any $y \in \mathbb{R}$. Due to the variation in size of the residues for high ℓ , Eq. (15) does not offer a viable means for such evaluation (even given the ability to compute the poles and residues), unless ℓ is low. However, numerical evaluation based on Eq. (42) (below) is well conditioned. Use of Eq. (42) amounts to a cumbersome offline step, through which we construct an accurate rational approximation $\hat{\Xi}_\ell(s, r_1, r_2)$ to $\hat{\Phi}_\ell(s, r_1, r_2)$ along the inversion contour. The approximate kernel $\hat{\Xi}_\ell(s, r_1, r_2)$ typically has $d \ll \ell$ poles for large ℓ , and is therefore a "compression" of the exact ℓ -pole kernel. Quite remarkably, (approximate) evaluation of $\hat{\Phi}_\ell(iy, r_1, r_2)$ based on the d -pole sum $\hat{\Xi}_\ell(iy, r_1, r_2)$ is much better conditioned than evaluation based on the exact ℓ -pole sum (15).

3.1 Profile evaluation

We now describe our alternate approach for evaluation of the profiles $\text{Re}\hat{\Phi}_\ell(iy, r_1, r_2)$ and $\text{Im}\hat{\Phi}_\ell(iy, r_1, r_2)$ for $y \in \mathbb{R}$. As mentioned, Ref. [4] has described stable evaluation of the *time-domain* kernel $\Phi_\ell(t, r_1, r_2)$. Our approach is based on the following expression for a teleportation kernel [3]:

$$\hat{\Phi}_\ell(s, r_1, r_2) = -1 + \underbrace{\exp\left[\int_{r_1}^{r_2} \frac{\hat{\Omega}_\ell(s, \eta)}{\eta} d\eta\right]}_{W_\ell(sr_2)/W_\ell(sr_1)}, \quad (42)$$

where we have introduced an auxiliary function⁵

$$\hat{\Omega}_\ell(s, r) \equiv sr \frac{W'_\ell(sr)}{W_\ell(sr)} = \sum_{k=1}^{\ell} \frac{b_{\ell k}/r}{s - b_{\ell k}/r}, \quad (43)$$

with the prime indicating differentiation in argument. With Steed's algorithm [14] the kernel $\hat{\Omega}_\ell(s, r)$ is accurately computed via the known continued fraction expansion [14]

$$z \frac{W'_\ell(z)}{W_\ell(z)} = -\frac{\ell(\ell+1)}{2(z+1)+} \frac{(\ell-1)(\ell+2)}{2(z+2)+} \dots \frac{2(2\ell-1)}{2(z+\ell-1)+} \frac{2\ell}{2(z+\ell)}.$$

⁵ The kernel $\hat{\Omega}_\ell(s, r)$ arises when deriving exact outgoing (i.e. non-reflecting) boundary conditions. This interesting relationship expresses a teleportation kernel as a weighed integral over boundary kernels.

This formula follows from recurrence relations obeyed by MacDonald functions [13]. Given the ability to compute $\widehat{\Omega}_\ell(iy, r)$, computation of (42) can be carried out using numerical quadrature. Due to the parity of $\text{Re}\widehat{\Omega}_\ell(iy, r)$ (even in y) and $\text{Im}\widehat{\Omega}_\ell(iy, r)$ (odd in y), the numerical integrations involve no cancellation errors (i.e. the sums involve only positive or negative values at each fixed y_j grid point). We have found the representation (42) a useful tool for evaluation of high- ℓ teleportation kernels when evaluation based on the sum-of-poles representation (15) is inaccurate. Indeed, using quadruple precision arithmetic, we are typically able to evaluate the profiles $\text{Re}\widehat{\Phi}_\ell(iy, r_1, r_2)$ and $\text{Im}\widehat{\Phi}_\ell(iy, r_1, r_2)$ with relative errors well below double precision accuracy.

3.2 Compression

Kernel compression involves approximation of $\widehat{\Phi}_\ell(s, r_1, r_2)$ as a sum of (typically far) fewer poles. More precisely, given a prescribed error tolerance ε , consider the approximation⁶

$$\widehat{\Xi}_\ell(s, r_1, r_2) = \sum_{n=1}^d \frac{\gamma_{\ell n}(r_1, r_2)}{s - \beta_{\ell n}(r_1, r_2)}, \quad \sup_{s \in i\mathbb{R}} \left| \frac{\widehat{\Phi}_\ell(s, r_1, r_2) - \widehat{\Xi}_\ell(s, r_1, r_2)}{\widehat{\Phi}_\ell(s, r_1, r_2)} \right| < \varepsilon. \quad (45)$$

In fact, due to scaling relation (22) it suffices to consider only approximations for $1 \rightarrow r_2/r_1$ teleportation.⁷ However, in practice we construct compressions of generic $r_1 \rightarrow r_2$ kernels.

We now provide an error estimate associated with performing the convolution (16) with the compressed kernel $\Xi_\ell(t, r_1, r_2)$ given by (18) in place of the exact kernel $\Phi_\ell(t, r_1, r_2)$ given by Eq. (17). From the Parseval and Fourier convolution theorems, the relative convolution error stemming from a compressed kernel is [6, 3]

$$\begin{aligned} & \left\| \Xi_\ell(\cdot, r_1, r_2) * \Psi_{\ell m}(\cdot, r_1) - \Phi_\ell(\cdot, r_1, r_2) * \Psi_{\ell m}(\cdot, r_1) \right\|_{L_2(0, \infty)} \\ & \leq \sup_{s \in i\mathbb{R}} \frac{|\widehat{\Xi}_\ell(s, r_1, r_2) - \widehat{\Phi}_\ell(s, r_1, r_2)|}{|\widehat{\Phi}_\ell(s, r_1, r_2)|} \times \left\| \Phi_\ell(\cdot, r_1, r_2) * \Psi_{\ell m}(\cdot, r_1) \right\|_{L_2(0, \infty)}. \end{aligned} \quad (46)$$

Assuming a rational approximation which achieves (45), combination of (45) and (46) shows that the tolerance ε is a long-time bound on the relative convolution error.

We briefly describe our construction of compressed teleportation kernels. Provided that $r_2 - r_1$ is not too large, we use Algorithm 1 to produce a compressed kernel $\widehat{\Xi}_\ell(s, r_1, r_2)$. This is AGH compression, as described in [6, 7, 8, 9]. All of the kernels used in this article have been generated via a quadruple-precision implementation of this algorithm.

Algorithm 1 COMPUTATION OF A COMPRESSED TELEPORTATION KERNEL.

INPUT: $\ell, r_1, r_2, \varepsilon, N_C$ (number of composite subintervals), d (desired number of poles, possibly updated)

OUTPUT: $\{\beta_{\ell n}(r_1, r_2), \gamma_{\ell n}(r_1, r_2)\}_{n=1}^d$

- 1: Choose an approximation window $[-y_{\max}, y_{\max}]$ on the $\sigma = iy$ imaginary axis.
- 2: Partition $[-y_{\max}, y_{\max}]$ to form a y -grid $\{y_j\}_{j=1}^J$, typically with mesh refinement at the origin.
- 3: Numerically evaluate the profiles $\text{Re}\widehat{\Phi}_\ell(iy_j, r_1, r_2)$ and $\text{Im}\widehat{\Phi}_\ell(iy_j, r_1, r_2)$ on the y -grid via approximation of (42) using N_C -composite Gauss-Kronrad quadrature.
- 4: Compute the numbers $\{\beta_{\ell n}(r_1, r_2), \gamma_{\ell n}(r_1, r_2)\}_{n=1}^d$ by AGH compression; see Ref. [6]. The idea is to solve

$$\min_{\{\beta_{\ell n}(r_1, r_2), \gamma_{\ell n}(r_1, r_2)\}_{n=1}^d} \sum_{j=1}^J \mu_j \left| \widehat{\Phi}_\ell(iy_j, r_1, r_2) - \sum_{n=1}^d \gamma_{\ell n}(r_1, r_2) / (iy_j - \beta_{\ell n}(r_1, r_2)) \right|^2, \quad (47)$$

where μ_j are quadrature weights.

- 5: Using $\{\beta_{\ell n}(r_1, r_2), \gamma_{\ell n}(r_1, r_2)\}_{n=1}^d$, verify (45) for the chosen ε (typically on a different and finer y -grid). If not verified, repeat last two steps with $d \leftarrow d + 1$.

⁶ We correct several typos in Ref. [3]. In Eq. (37) of that reference, the second summation sign Σ should be a sup (supremum). Also in line 3 of **Algorithm 4**, each $\widehat{\omega}_2$ should be $\widehat{\omega}_\ell$.

⁷ Indeed, other scenarios are determined by the rules $\gamma_{\ell n}(r_1, r_2) = r_1^{-1} \gamma_{\ell n}(1, r_2/r_1)$ and $\beta_{\ell n}(r_1, r_2) = \beta_{\ell n}(r_1) = r_1^{-1} \beta_{\ell n}(1)$.

For reasons discussed in [3], when $r_2 \gg r_1$ Algorithm 1 becomes impractical. We therefore describe a modified procedure, assuming for simplicity that $r_1 = 1$ and $r_2 = 10^{P+1}$. We first compute the compressed kernel $\widehat{\Xi}_\ell^{(0)}(s, 1, 10) \equiv \widehat{\Xi}_\ell(s, 1, 10)$ using Algorithm 1. As suggested by the scaling relation (22), teleportation over decades $[10^p, 10^{p+1}]$ is then defined through

$$\widehat{\Xi}_\ell^{(p)}(s, 10^p, 10^{p+1}) = \widehat{\Xi}_\ell^{(0)}(s10^p, 1, 10) = \sum_{n=1}^d \frac{10^{-p}\gamma_{\ell n}(1, 10)}{s - 10^{-p}\beta_{\ell n}(1, 10)}. \quad (48)$$

Finally, we perform the evaluations more cheaply in step 3 of Algorithm 1 using a different formula,

$$\widehat{\Phi}_\ell(iy_j, 1, 10^{P+1}) \simeq -1 + \prod_{p=0}^P [1 + \widehat{\Xi}_\ell^{(p)}(iy_j, 10^p, 10^{p+1})]. \quad (49)$$

Here a collection of compressed kernels is combined to generate profiles from which one new compressed kernel is obtained.

3.3 Error estimate for pole-sum approximations

We have used Algorithm 1 (or its elaboration discussed in the last subsection) to construct compressed kernels. In view of the error estimate (46), we wish to know (or bound) the maximum pointwise error associated with a compressed kernel. To estimate this error in practice, we have resorted to numerical comparison between the compressed kernel and the "truth" kernel; see Subsection 4.1. However, here we describe an a priori estimate for the relevant pointwise error.

Consider a sum $f(z)$ of n simple poles. The function $f(z)$ may represent one of our frequency domain kernels, although here we use z in place of s as the independent variable. Provided that evaluation of $f(z)$ is restricted to z -values which are sufficiently separated from the pole locations $\{z_i\}_{i=1}^n$, a sum $g(z)$ of $d < n$ simple poles may accurately approximate $f(z)$. Reference [6] analyzes this issue, giving both explicit constructions and error bounds. Such constructions are not used in Algorithm 1. Nevertheless, they demonstrate that good approximations exist and may shed light on observed numerical behavior (cf. Subsection 4.2).

Lemma 1 *Suppose $\{q_j, z_j\}_{j=1}^n$ are n complex pairs defining the function $f(z) = \sum_{j=1}^n q_j/(z - z_j)$, with all locations z_j contained in the union of p disks D_1, \dots, D_p . The disk D_k has radius r_k and is centered at c_k . There exists an approximation $g(z)$, itself a sum of $d = m \cdot p$ simple poles, which obeys the estimate*

$$|f(z) - g(z)| \leq \frac{K(a^2 + 1)}{(a^m - 1)(a - 1)^2} \left| \sum_{j=1}^n \frac{|q_j|}{|z - z_j|} \right|, \quad z \in \mathcal{U}_a \equiv \{z | \operatorname{Re}(z - c_k) \geq ar_k > r_k, 1 \leq k \leq p\}, \quad (50)$$

where the constant K is independent of a .

For disks in the left-half plane we choose the largest $a > 1$ such that \mathcal{U}_a contains the inversion contour (i.e. the imaginary axis). Provided n is sufficiently large, the estimate (50) indicates that the error decays exponentially with the number $m \cdot p$ of poles. For an index- ℓ radiation boundary kernel, the residues and pole locations are $q_j = b_{\ell j} = z_j$, assuming a unit-sphere physical boundary. Since $b_{\ell j} \sim \ell$ for large- ℓ , these kernels correspond to a bound (50) which scales mildly with ℓ . For an index- ℓ teleportation kernel (with $r_1 = 1$) the locations are again $z_j = b_{\ell j}$; however, now the residues $q_j = a_{\ell j}$ scale exponentially with ℓ , maring the bound (50). Nevertheless, Section 4 demonstrates that Algorithm 1 yields accurate large- ℓ approximate kernels.

The discussion above serves to raise the following points. (i) Despite the fact that the kernels for radiation boundary conditions and teleportation share pole locations, teleportation kernels should be harder to approximate. (ii) Regardless, for fixed ℓ , approximations with exponential accuracy exist in principle. (iii) For both types of kernels the set of pole locations can be covered by $p \propto \log \ell$ disks (Ref. [6] uses this p for RBC kernels). (iv) In the bound (50) the exponential growth of the residues $q_j = a_{\ell j}$ with ℓ suggests that to achieve an approximation with a fixed error tolerance the number d of poles needs to scale linearly with ℓ . Subsection 4.2 presents numerical evidence supporting this heuristic observation. A problem whose solution might address the conditioning of our approximations would be to bound the largest and smallest residues (in modulus) for a given $g(z)$, and further to understand how these bounds scale with ℓ . Subsection 4.2 empirically addresses some of these issues.

4 Example compressed kernels, empirical scalings, and numerical experiments

Our first subsection describes approximation of large- ℓ frequency-domain kernels. Our goal is the construction of compressed kernels, each with poles and residues that, when stored in double precision scientific format, yield accurate evaluation of the kernel along the inversion contour. Our second subsection summarizes empirical scaling relations between ℓ , d , r_2 , r_1 , $\max_j |\gamma_{\ell j}|$, and ε . In the last subsection two experiments describe signal teleportation. These experiments evolve time-domain multipole $\Psi_{\ell m}(t, r)$ which obey (6). Working with the one-dimensional radial wave equation allows us to more easily focus on the errors associated with the kernels as opposed to computational grid discretization error. Teleportation schemes implemented within three-dimensional time-domain wave equation solvers would require spherical harmonic transformation to compute each multipole.

4.1 Example compressions of large- ℓ kernels

We first consider $\ell = 64$, with teleportation from either $r_1 = 15, 30, 60$, or 120 to $r_2 = 240$. Due to the scaling relation (22) these cases are similar to teleportation from $r_1 = 1$ to $r_2 = 16, 8, 4, 2$. Figure 2 shows the real and imaginary profiles associated with the kernel $\hat{\Phi}_{64}(s, 15, 240)$ along the inversion contour. Based on (31), we expect that the exact residues $a_{64,j}(15, 240)$ corresponding to the kernel $\hat{\Phi}_{64}(s, 15, 240)$ vary in modulus over 15 orders of magnitude, with the largest residue $\gtrsim 10^{15}$ in modulus. Therefore, one expects that a table of the poles and residues specifying $\hat{\Phi}_{64}(s, 15, 240)$ would, if formatted in double precision, yield few digits of accuracy. Nevertheless, perhaps somewhat paradoxically, we will demonstrate that the kernel $\hat{\Phi}_{64}(iy, 15, 240)$ can be uniformly approximated for $y \in \mathbb{R}$ by a sum of *fewer poles*.

Table 1 summarizes our best compressions for all four choices of r_1 , and we find that between 30 and 34 poles are sufficient to achieve $\varepsilon \lesssim 1.0 \times 10^{-10}$. To estimate the error tolerance ε in (45) each approximate kernel is compared against the "truth" kernel (i.e. numerical evaluation of $\hat{\Phi}_{64}(iy, r_1, 240)$ with (42)) relative to a dense reference grid with logarithmic refinement. In estimating ε , we also change the parameters for numerical quadrature used in evaluation of the "truth" kernel, thereby avoiding systematic errors. Reference [3] has also examined compressed kernels approximating $\hat{\Phi}_{64}(s, 15, 240)$, in particular plotting the pole locations for $d = 20, 28$, and 36 compressed kernels. Figure 3 of that reference compares the pole locations of compressed teleportation and RBC kernels. For both types of compressed kernel as d increases (corresponding to smaller ε), more of the d pole locations "lock on" to the transcendental curve shown in Fig. 1.

r_1	d	ε	$\min_j \gamma_{64,j}(r_1, 240) $	$\max_j \gamma_{64,j}(r_1, 240) $	$\min_j a_{64,j}(r_1, 240) $	$\max_j a_{64,j}(r_1, 240) $
15	34	1.0×10^{-10}	8.5972×10^{-3}	1.3898×10^6	1.9086×10^1	4.3234×10^{15}
30	32	1.0×10^{-11}	1.1253×10^{-2}	4.2480×10^5	7.6889×10^0	1.0431×10^{14}
60	30	5.0×10^{-11}	1.7761×10^{-2}	7.2223×10^4	2.4873×10^0	1.3124×10^{11}
120	30	5.0×10^{-12}	7.2560×10^{-2}	3.7582×10^3	4.8933×10^{-1}	7.4516×10^5

Table 1 INFORMATION FOR $\ell = 64$ COMPRESSED KERNELS. Note that the min/max values for $|a_{64,j}(r_1, 240)|$ have been computed with (30). Values computed with the asymptotic expansion (31) are the same to about 3 digits of relative accuracy.

As a more extreme example, consider the teleportation kernel $\hat{\Phi}_{256}(iy, 15, 240)$ shown in Fig. 3. Based on (31), we expect the residues $a_{256,j}(15, 240)$ to vary in modulus over 64 orders of magnitude, with the largest residue $\gtrsim 10^{67}$ in magnitude. Therefore, a table based on storage of the exact poles and residues in double precision format likely yields no digits of accuracy. Nevertheless, we have found that a compressed kernel with $d = 72$ poles, when stored in double precision format, corresponds to $\varepsilon \lesssim 5.0 \times 10^{-8}$; moreover, storage of a $d = 79$ compressed kernel in quadrupole precision format corresponds to $\varepsilon \lesssim 5.0 \times 10^{-11}$.

4.2 Empirical scalings

We have carried out 1183 independent kernel compressions over the parameters $(\ell, d, \varepsilon, r_2/r_1)$, and with these explore relevant scalings for our approximations. Figures 4 to 8 summarize the results. Unless stated otherwise, all experiments in this subsection vary r_1 with $r_2 = 240$ fixed. Results for $r_1 = 15$ fixed and varying r_2 are in most cases qualitatively similar. We are primarily interested in the first approach to varying r_2/r_1 , since it comports with teleportation as a technique for asymptotic waveform evaluation [3], although typically $r_2 \gg 240$ in that context. Each compression has

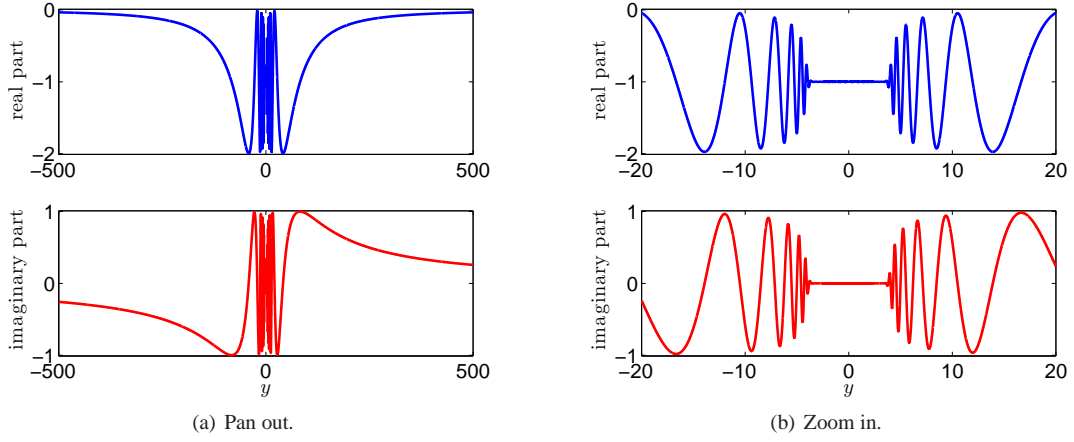


Fig. 2 Teleportation kernel $\widehat{\Phi}_{64}(iy, 15, 240)$. The upper plots depict $\text{Re}\widehat{\Phi}_{64}(iy, 15, 240)$ and the bottom plots $\text{Im}\widehat{\Phi}_{64}(iy, 15, 240)$.

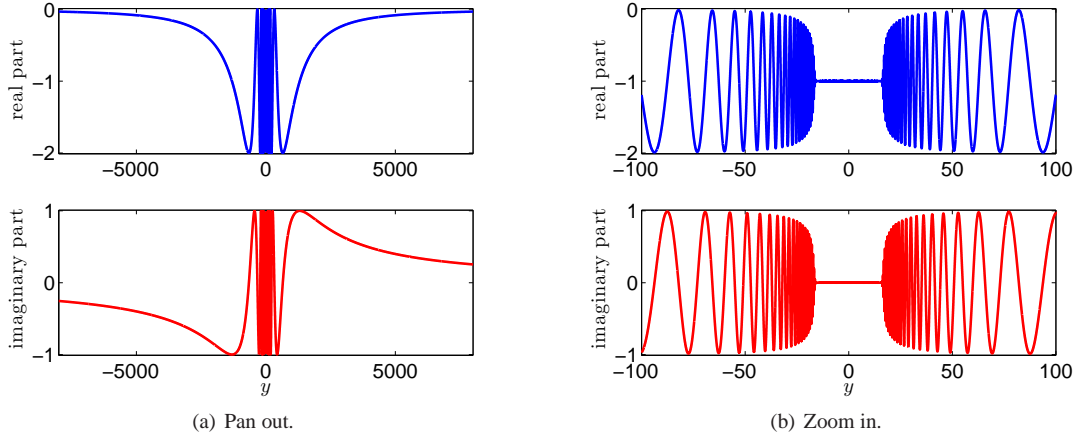


Fig. 3 Teleportation kernel $\widehat{\Phi}_{256}(iy, 15, 240)$. The upper plots depict $\text{Re}\widehat{\Phi}_{256}(iy, 15, 240)$ and the bottom plots $\text{Im}\widehat{\Phi}_{256}(iy, 15, 240)$.

been computed in quadruple precision arithmetic, with the resulting pole locations and residues stored in both double and quadruple precision formats. For smaller ℓ values we have used the double precision format without loss of accuracy. However, in some cases (e.g. $\ell = 128, 256$) below, we have found it necessary to use the quadruple precision format to retain high accuracy.

4.2.1 Scaling of compressed-kernel pole number d with compression error ε

Figure 4(left) confirms the exponential decay of the approximation suggested by Lemma 1. These plots indicate that for fixed values of ℓ and r_2/r_1 , the number d of approximating poles scales like

$$d = O(\log(1/\varepsilon)). \quad (51)$$

4.2.2 Scaling of compressed-kernel pole number d with spherical-harmonic index ℓ

Figure 5 depicts the growth of the compressed-kernel pole number d with spherical-harmonic index ℓ . For fixed values of r_1 and r_2 , the number of approximating poles is best described by the fit

$$d = a_1 + a_2 \log(\ell) + a_3 \ell. \quad (52)$$

As judged by standard goodness-of-fit statistics, Eq. (52) models the growth of d better than solely log, linear, or \log^2 scaling. Formally then, d would appear to be $O(\ell)$ for large ℓ . However, for small and medium ℓ the logarithmic term dominates, and, furthermore, the coefficient a_2 is typically small. For example, the fits shown in Fig. 5(left) are as follows.

$$\begin{aligned} r_2/r_1 = 16: & \quad a_1 = -7.814, \quad a_2 = 5.112, \quad a_3 = 0.1621 \\ r_2/r_1 = 8: & \quad a_1 = -4.096, \quad a_2 = 4.017, \quad a_3 = 0.1596 \\ r_2/r_1 = 4: & \quad a_1 = 0.1785, \quad a_2 = 2.537, \quad a_3 = 0.1551 \\ r_2/r_1 = 2: & \quad a_1 = -3.449, \quad a_2 = 3.435, \quad a_3 = 0.0994 \end{aligned}$$

The scaling (52) is at odds with the conjecture made in Ref [3] just after Eq. (40) of that reference.

4.2.3 Scaling of largest residue $\max_j |\gamma_{\ell j}|$ with compression error ε

Figure 6 depicts the growth of the compressed-kernel maximum residue (in modulus) with the approximation. These plots indicate that for fixed values of ℓ , r_1 , and r_2 the largest residue scales like

$$\max_j |\gamma_{\ell j}| = O(\log(1/\varepsilon)). \quad (53)$$

We anticipate that $\max_j |\gamma_{\ell j}|$ approaches $\max_j |a_{\ell j}|$ as $d \rightarrow \ell$, since the best ℓ -pole approximation of the kernel would be the kernel itself. Due to the high precision required we are unable to probe the regime $d \approx \ell$ in the large- ℓ limit.

4.2.4 Scaling of largest residue $\max_j |\gamma_{\ell j}|$ with spherical-harmonic index ℓ

Figure 7(left) depicts the growth of the compressed-kernel maximum residue (in modulus) with spherical-harmonic index ℓ . For fixed values of r_1 , r_2 , and ε the data is well modeled by

$$\max_j |\gamma_{\ell j}| = \exp(a_1 \log(\ell) + a_2). \quad (54)$$

The fits shown in Fig. 7(left) are as follows.

$$\begin{aligned} r_2/r_1 = 16: & \quad a_1 = 5.58, \quad a_2 = -11.09 \\ r_2/r_1 = 8: & \quad a_1 = 5.57, \quad a_2 = -12.20 \\ r_2/r_1 = 4: & \quad a_1 = 5.75, \quad a_2 = -14.57 \\ r_2/r_1 = 2: & \quad a_1 = 5.80, \quad a_2 = -18.14 \end{aligned}$$

Figure 7(right) depicts the growth of the exact-kernel maximum residue (in modulus), as computed by (31).

4.2.5 Scaling of largest residue $\max_j |\gamma_{\ell j}|$ with r_2/r_1

Figure 8 depicts the growth of the compressed-kernel maximum residue (in modulus) with r_2/r_1 . We consider two cases: (i) r_2 fixed (left) and (ii) r_1 fixed (right). Notice that the maximum residue grows more quickly as $r_1 \rightarrow 0$ than it does as $r_2 \rightarrow \infty$. This observation is expected. Indeed, for case (i) the effective potential $\ell(\ell+1)r_1^{-2}$ at r_1 grows without bound as $r_1 \rightarrow 0$. Whence increasing r_2/r_1 corresponds to propagation from a region of increasingly large potential. However, for case (ii) similar considerations show that increasing r_2/r_1 corresponds to propagation into a region of increasingly small potential. Regardless, the limiting case $r_2 \rightarrow \infty$ does not appear problematic for those cases considered. Furthermore, Ref. [3] has achieved high accuracy kernel compressions for $r_2 \simeq 10^{15}$ (albeit for low- ℓ and the wave equations describing gravitational perturbations).

4.3 Pulse teleportation

This subsection presents an experiment similar to the one carried out in [3] for the Regge-Wheeler equation (see the conclusion). We take $\ell = 64$ with Gaussian initial data:

$$\Psi(0, r) = e^{-(r-8)^2}, \quad \partial_t \Psi(0, r) = -\partial_r \Psi(0, r), \quad (55)$$

where we have suppressed the $(\ell = 64, m)$ indices on Ψ . Using a multidomain nodal Chebyshev method (described in [15]), we perform five separate evolutions on domains with outer boundaries $b = 15, 30, 60, 120, 240$. We have

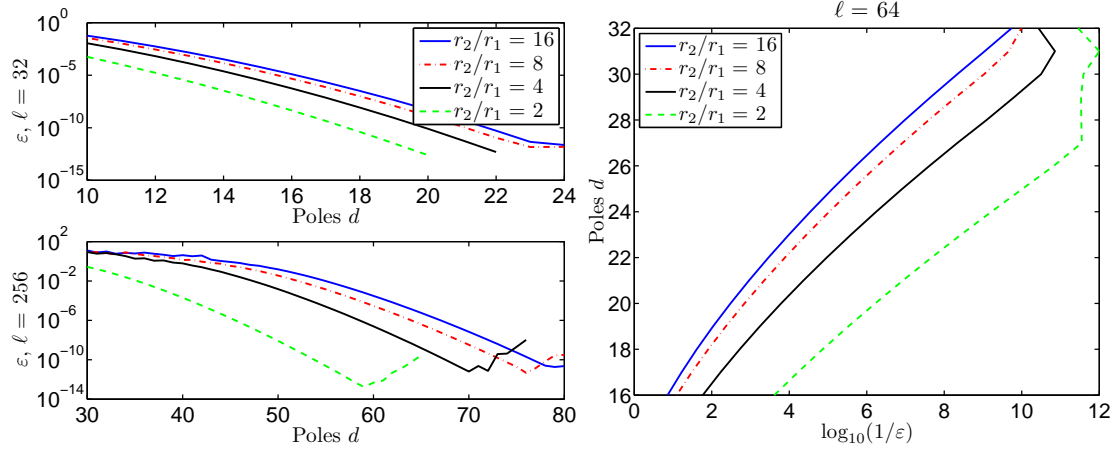


Fig. 4 Exponential decay of compression error ε with pole number d . Plots for other ℓ values are qualitatively similar.

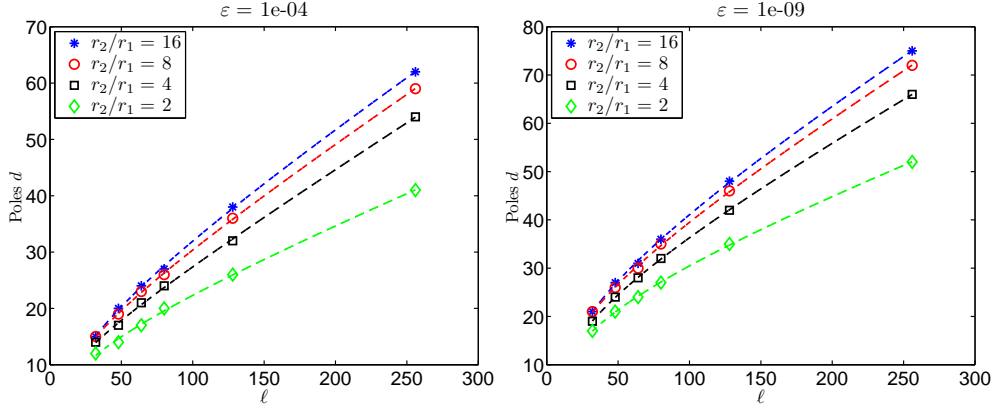


Fig. 5 Growth of pole number d with spherical-harmonic index ℓ . Plots for other values of ε are qualitatively similar. Fits described by (52) correspond to the dashed lines.

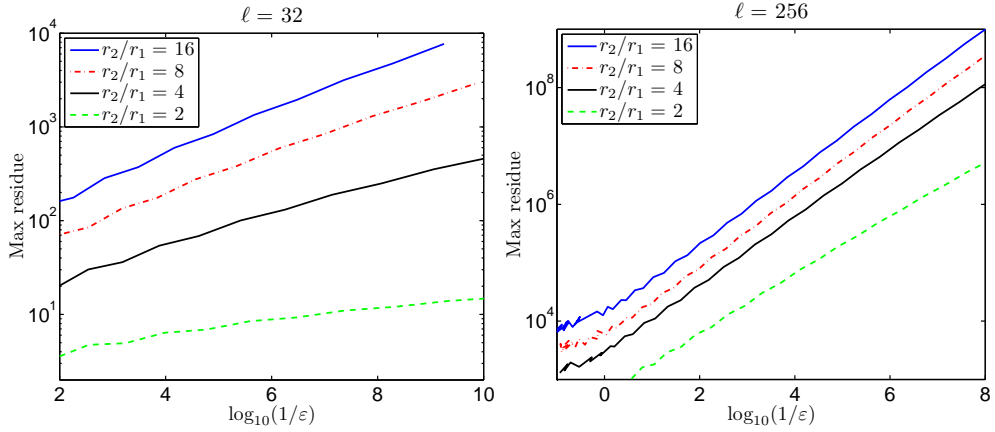


Fig. 6 Growth of compressed-kernel largest residue $\max_j |\gamma_{\ell j}|$ with compression error ε .

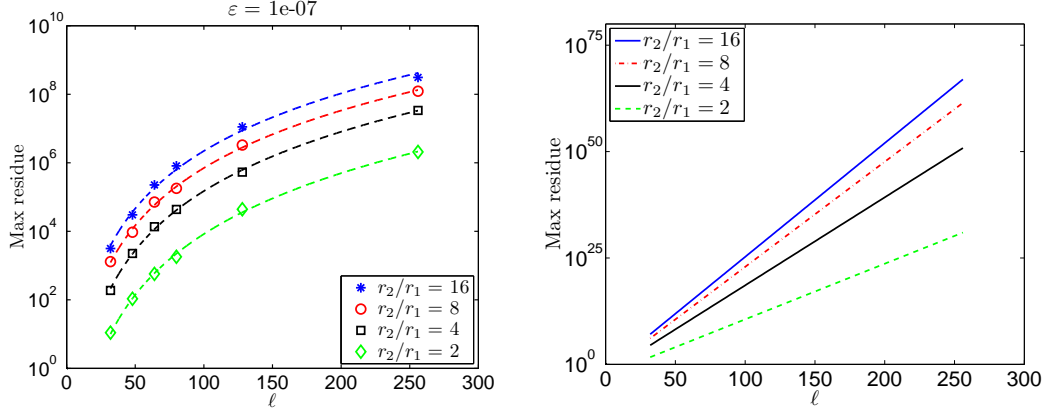


Fig. 7 Growth of compressed-kernel largest residue $\max_j |\gamma_{\ell j}|$ with spherical-harmonic index ℓ . Results for four families of $\varepsilon = 10^{-7}$ kernels are shown(left), with the dashed lines showing fits to the data as described by Eq. (54). For comparison, the corresponding results for the exact-kernel $\max_j |a_{\ell j}|$ are also shown(right).

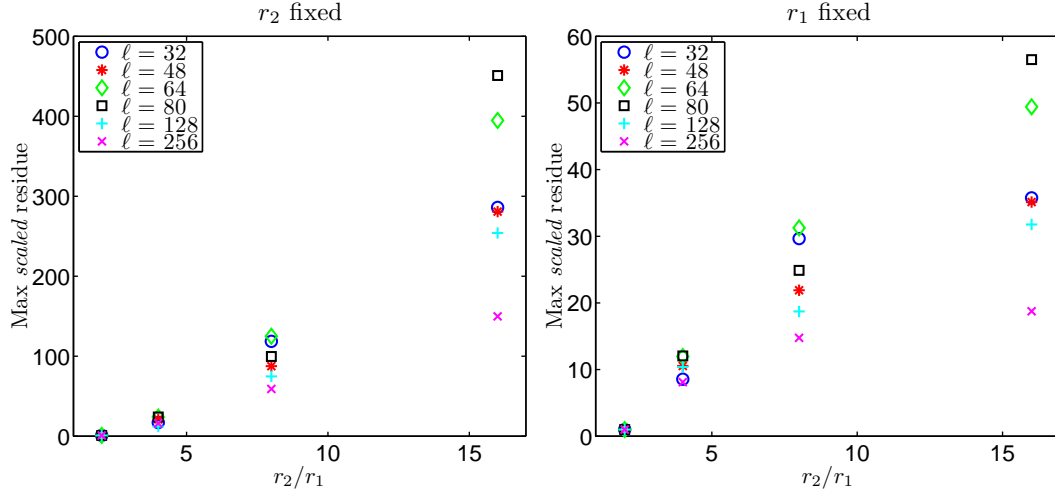


Fig. 8 Growth of compressed kernel's largest residue with pole number r_2/r_1 . For plotting convenience a scaled maximum residue is shown. The scaling factor is chosen such that the maximum residue is 1 at $r_2/r_1 = 2$, thereby ensuring similar residue magnitudes among the different ℓ kernels.

respectively used 8, 16, 30, 60, and 120 subintervals of uniform size, and in each case with 42 Chebyshev-Lobatto points per subinterval. Therefore, the spatial resolution for each evolution is comparable to the others. Evolutions are performed by the classical 4-stage explicit Runge Kutta method with timestep $\Delta t \simeq 4.0461e-05$. For each evolution the inner boundary is $a = 2$, at which we have enforced a Sommerfeld boundary condition $\partial_t \Psi - \partial_r \Psi = 0$. For all choices of outer boundary b we adopt the Laplace convolution radiation boundary conditions (RBC) based on (compressed kernels for) the time-domain kernel $\Omega_{64}(t, b)$ (see [3] for more detail). Tables for the $b = 15, 20, 60, 120, 240$ RBC respectively have 19, 19, 19, 18, and 17 poles, with each table computed in quadruple precision to satisfy the tolerance $\varepsilon = 10^{-15}$.

In all five simulations the field $\Psi(t, b)$ is recorded as a time series at the boundary b , and in all cases but $b = 240$ we "teleport" the field from $r_1 = b$ to $r_2 = 240$. The compressed teleportation kernels $\Xi_{64}(t, b, 240) \simeq \Phi_{64}(t, b, 240)$ have been described in the previous subsection. For the $b = 240$ simulation we simply record the field at the boundary, with this record then serving as a reference time series. We account for time delays by starting all recorded times series (whether read off or teleported) at time $b - 12$. The top panel in Figure 9 plots the errors in the waveforms recorded at the different b boundaries as compared to the reference $b = 240$ waveform; as expected the systematic errors are large. The bottom panel plots the errors in the $r_1 = b \rightarrow r_2 = 240$ teleported time series relative to the reference time series.

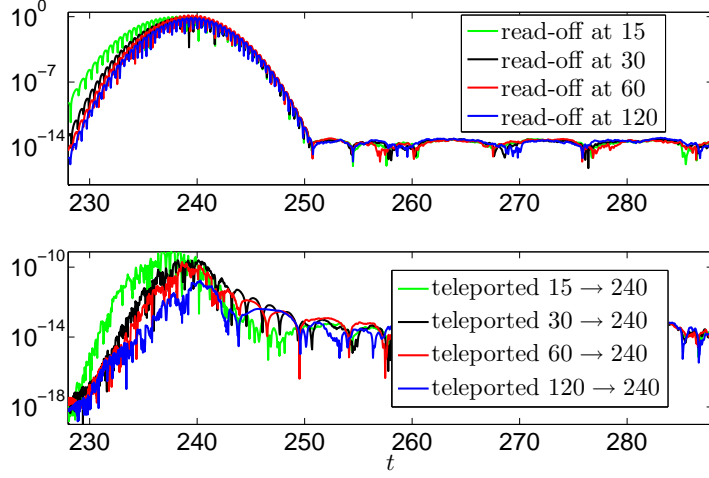


Fig. 9 Teleportation of an $\ell = 64$ Gaussian pulse. Here all errors have been computed against the reference signal read-off at $r = 240$. The top panel then compares the reference signal with the signals read-off at $r = 15, 30, 60, 120$. The bottom panel compares the reference signal with the signals obtain through teleportation from $r_1 = 15, 30, 60, 120$ to $r_2 = 240$.

4.4 Asymptotic-waveform evaluation

We now consider asymptotic-waveform evaluation (AWE) by teleportation of a pure $\ell = 2$ multipole signal recorded from $r_1 = 10$ to $r_2 = \infty$. From (15) the $\ell = 2$ frequency-domain teleportation kernel is

$$\hat{\Phi}_2(s, r_1, r_2) = \frac{a_{21}(r_1, r_2)}{s - z_-/r_1} + \frac{a_{22}(r_1, r_2)}{s - z_+/r_1}, \quad z_{\pm} = -\frac{3}{2} \pm i\frac{\sqrt{3}}{2}, \quad (56)$$

where $W_2(z_{\pm}) = 0$ and $b_{21} = z_-$, $b_{22} = z_+$. The AWE residues can be found through direct evaluation of (21), giving

$$\Phi_2(t, 10, \infty) = \tilde{a} \exp\left(\frac{z_-}{10}t\right) + \tilde{a}^* \exp\left(\frac{z_+}{10}t\right), \quad \tilde{a} = -i\frac{\sqrt{3}}{30}z_-^2, \quad (57)$$

as the relevant time-domain AWE kernel and where we make use⁸ of $a_{22} = a_{21}^*$.

We now use the AWE kernel (57) to recover the asymptotic solution from a recorded time-series. To directly compute errors, we shall consider an exact, closed-form solution. From Eq. (9) the general $\ell = 2$ outgoing solution to Eq. (6) is

$$\Psi(t, r) = f''(t - r) + \frac{3}{r}f'(t - r) + \frac{3}{r^2}f(t - r), \quad (58)$$

where $f(u)$ is an underlying function of retarded time $u = t - r$, the prime indicating differentiation in argument, and we have suppressed the $(\ell = 2, m)$ indices on Ψ . The specification

$$f(u) = \sin[f_0(u - u_0)]e^{-c(u - u_0)^2}, \quad (59)$$

determines a purely outgoing multipole solution whose asymptotic signal is

$$\Psi_{\infty}(T) \equiv \left[-4cf_0T \cos(f_0T) + (-2c - f_0^2 + 4c^2T^2) \sin(f_0T) \right] e^{-cT^2}, \quad T \equiv t - r_1 - u_0. \quad (60)$$

Here c characterizes the solution's spatial extent, f_0 its "central" frequency, and u_0 its offset. To obtain (60), we have adjusted for the infinite time delay for the signal to reach $r_2 = \infty$. Indeed, the signal at (t_1, r_1) reaches r_2 at time $t_1 + (r_2 - r_1)$; both correspond to the retarded time $u_1 = t_1 - r_1$ (the combination in T) even for $r_2 = \infty$. For all experiments we choose $f_0 = 1$, $c = 2.5$, and $u_0 = -6$. To distinguish from exact solutions, we append a subscript h to any quantity obtained with our multidomain nodal Chebyshev solver.

⁸ For even ℓ the residues come in conjugate pairs, as seen from (21) and the fact that the roots $b_{\ell j}$ also come in conjugate pairs.

The numerical setup is similar that of Sec. 4.3, except that we now choose 22 Chebyshev-Lobatto points on 8 subintervals and $\Delta t \simeq 5.3949\text{e-}05$. Initial data is found from Eq. (58) and its spatial and temporal derivatives, all evaluated at $t = 0$. The signal $\Psi_h(t, 10)$ recorded at $r_1 = 10$ is the solid black line in Fig. 10(a). With this data we compute $\Psi_{\infty,h}(T)$, the dashed red line in Fig. 10(a), from the convolution (16) with kernel (57). In numerical studies, often the outermost recorded signal is taken to be the asymptotic one. The dash-dot blue line in Fig. 10(a) plots the *systematic error* $\Psi_{\infty,h}(T) - \Psi_h(t, 10)$, with multiplication by 10 as a visual aid. Notice that the systematic error is $O(1/r_1)$, in accord with Eq. (58).

The difference between the exact asymptotic signal $\Psi_{\infty}(T)$ and our numerically teleported one is the dashed red line in Fig. 10(b). As the exact AWE kernel has been used with teleportation convolution that is accurately evaluated for our choice of Δt , these errors must stem from the numerical solver. This expectation is confirmed by the solid black line in Fig. 10(b) which plots the error $\Psi(t, 10) - \Psi_h(t, 10)$.

When teleportation is carried out to a large radial value, performance of a convergence test on a commensurately larger computational domain becomes unfeasible. Such is the case here, but Eq. (63) from the appendix provides a useful error bound for $\Psi_{\infty}(T) - \Psi_{\infty,h}(T)$ in terms of $\Psi(t, 10) - \Psi_h(t, 10)$, where the latter error can be estimated through a convergence study. The dashed red line in Fig. 11 plots this error bound versus the number of Chebyshev-Lobatto points used in our computation and sharply bounds the solid black line which depicts the exact error.

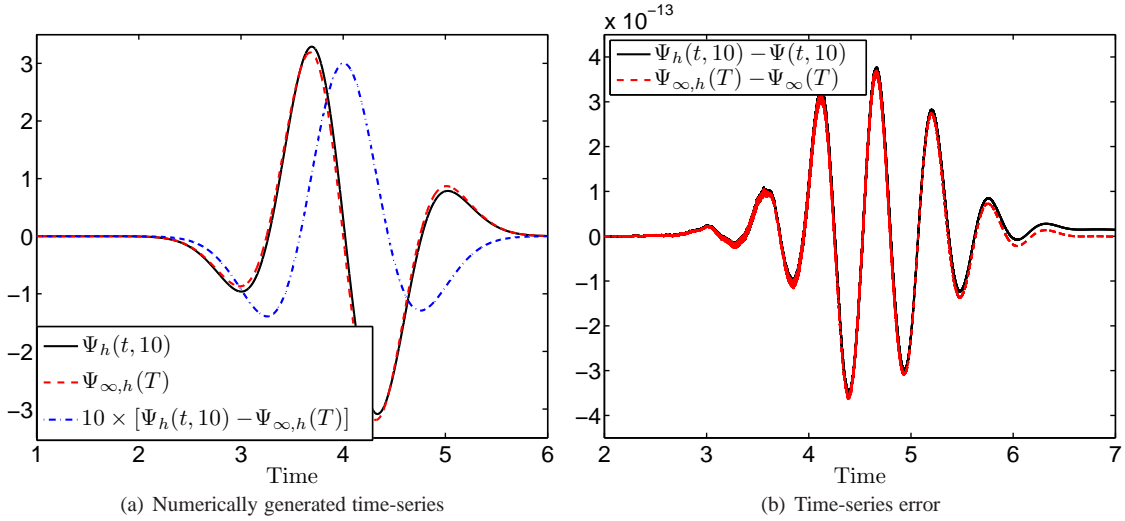


Fig. 10 The left plot depicts the $r_1 = 10$ recorded data (solid black line) and its teleportation to $r_2 = \infty$ (dashed red line). The difference between these time-series (dash-dot blue line) characterizes the systematic error engendered by approximation of the true asymptotic signal by the finite-radial value one. For visual assistance, we have multiplied this error by 10. The right figure depicts the numerical errors which have been computed relative to the exact time-series.

5 Concluding remarks

For solutions to the ordinary 3-space dimensional wave equation, we have described exact teleportation of a time-domain multipole signal recorded at r_1 to another radial location r_2 , thereby recovering the signal which would eventually reach r_2 . We have focused on three issues, presenting new results for each. First, we have described the structure of the exact convolution kernels which define such teleportation, and the large- ℓ (polar spherical harmonic index) cancellation errors associated with their exact sum-of-poles representations (in finite-precision arithmetic). In particular, we have given a slightly more detailed derivation of Greengard, Hagstrom, and Jiang's result for the large- ℓ asymptotics of the residues. Second, we have described an accurate procedure, based on the work in Ref. [3], for sphere-to-sphere signal propagation for the ordinary wave equation. The key ingredients of the procedure are (i) accurate evaluation of frequency-domain kernels through the algorithm described in section 3.1 and (ii) rational approximation (i.e. kernel compression) of these kernels through the algorithm described in section 3.2. Lacking precise theoretical understanding of compressed teleportation kernels, we have modeled (from numerical data) the relationships between the parameters

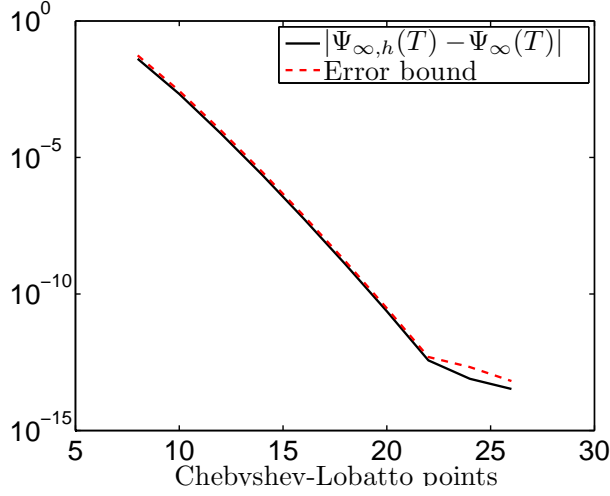


Fig. 11 The exact (solid black line) and estimated (dashed red line) error from Eq. (63). To form this bound we compute $\|\Phi_2(\cdot, 10, \infty)\|_{L_\infty} = \frac{3}{10}$ from Eq. (64).

determining these approximations. As suggested in Ref. [4], the kernel representations derived in Ref. [4] might be compressed using only the rational approximation step, thereby reducing the cost of their evaluation. The compressions reported here indicate that this strategy is possible, at least through $\ell = 256$. Finally, we have focused on practical implementation, demonstrating through simulations that teleportation can be performed accurately.

While this article has presented results only for the ordinary wave equation (4), our methods can be extended to certain other hyperbolic PDEs, including those posed on non-flat geometries for which backscatter effects make the separation of "ingoing" and "outgoing" waves particularly vexing. Indeed, the main motivation for this work has been to compute asymptotic gravitational wave signals [3]. Here the governing equations are those of Regge-Wheeler and Zerilli, respectively describing axial and polar perturbations of spherically symmetric blackholes. We are unaware of closed-form time-domain representations for the asymptotically outgoing solutions to these equations. Moreover, Laplace transforms of the corresponding (boundary and teleportation) kernels feature branch cuts in their domains of analyticity [16]. Nevertheless, our approach carries over to this more complicated gravitational scenario. The idea is to again base kernel compression on evaluation of the exact kernel through (42) (other numerical techniques are also required [17]). Based on this work, we conjecture that the methods described here can be applied to linear hyperbolic systems which (apart from inhomogeneities) are time independent and rotationally invariant. Extension of these methods to systems with spheroidal invariance is an open problem.

Finally, we note that compressed kernels are available at [18]. To date, we have mostly posted radiation boundary and teleportation kernels for the Regge-Wheeler and Zerilli equations. However, we intend to add the kernels used in the numerical experiments documented here.

6 Acknowledgements

SRL gratefully acknowledges support from NSF grant No. PHY 0855678 to the University of New Mexico, with which infrastructure for our approximations was developed. SEF acknowledges support from the Joint Space Science Institute and NSF Grants No. PHY 1208861 and No. PHY 1005632 to the University of Maryland, NSF Grants PHY-1306125 and AST-1333129 to Cornell University, and by a grant from the Sherman Fairchild Foundation. For insights and helpful comments we wish to thank Thomas Hagstrom and Akil Narayan.

A The conditioning and error bounds of teleportation with respect to data perturbation

We now consider conditioning of teleportation with respect to data perturbation and related error bounds. In this appendix (ℓ, m) indices and, often, radial arguments r_1, r_2 on Ψ and Φ are suppressed. Let

$$\Phi * \delta\Psi(t) = \int_0^t \Phi(t-t')\delta\Psi(t')dt', \quad t \in [0, T]. \quad (61)$$

Here $\delta\Psi(t', r_1) = \Psi(t', r_1) - \Psi_h(t', r_1)$ is the time-series error due to numerical discretization, and T is the final time. One version of Young's convolution inequality yields

$$\|\Phi * \delta\Psi\|_{L_\infty(0,T)} \leq \|\Phi\|_{L_\infty(0,T)} \cdot \|\delta\Psi\|_{L_1(0,T)}, \quad (62)$$

which with (16) immediately gives (upon replacing the radial arguments)

$$\|\Psi(\cdot + (r_2 - r_1), r_2) - \Psi_h(\cdot + (r_2 - r_1), r_2)\|_{L_\infty(0,T)} \leq \|\Phi(\cdot, r_1, r_2)\|_{L_\infty(0,T)} \cdot \|\delta\Psi(\cdot, r_1)\|_{L_1(0,T)} + \|\delta\Psi(\cdot, r_1)\|_{L_\infty(0,T)}. \quad (63)$$

Numerical evidence suggests [4] that $|\Phi_\ell(t, r_1, r_2)|$ is maximal at $t = 0$. Furthermore,

$$\Phi_\ell(0, r_1, r_2) = \frac{1}{r_1} \left[\frac{\ell(\ell+1)}{2} \left(\frac{r_1}{r_2} - 1 \right) \right], \quad (64)$$

which follows from Lemma 1 of Ref. [4] and the scaling relation (22).

References

1. C. H. Wilcox, *The initial-boundary value problem for the wave equation in an exterior domain with spherical boundary*, Notices Amer. Math. Soc. 6 (1959) 869-870.
2. T. Tokita, *Exponential decay of solutions for the wave equation in the exterior domain with spherical boundary*, J. Math. Kyoto Univ. 12-2 (1972) 413-430.
3. A. G. Benedict, S. E. Field, S. R. Lau, *Fast evaluation of asymptotic waveforms from gravitational perturbations*, Class. Quantum Grav. 30, 055015 (2013) [35 pages].
4. L. Greengard, T. Hagstrom, and S. Jiang, *The solution of the scalar wave equation in the exterior of a sphere*, J. Comput. Phys. 274, issue 0 (2014) 191-207; arXiv:1308.0643 [math.NA].
5. M. J. Grote and J. B. Keller, *Nonreflecting Boundary Conditions for Time-Dependent Scattering*, J. Comput. Phys. 127, issue 1 (1996) 52-65.
6. B. Alpert, L. Greengard, and T. Hagstrom, *Rapid Evaluation of Nonreflecting Boundary Kernels for Time-Domain Wave Propagation*, SIAM J. Numer. Anal. 37 (2000) 1138-1164.
7. S. Jiang, *Fast Evaluation of Nonreflecting Boundary Conditions for the Schrödinger Equation*, New York University Ph. D. Dissertation (2001).
8. K. Xu and S. Jiang, *A Bootstrap Method for Sum-of-Poles Approximations*, J. Sci. Comput. 55, issue 1 (2013) 16-39.
9. D. A. Bizzozero, J. A. Ellison, K. A. Heinemann, and S. R. Lau, *Rapid evaluation of two-dimensional retarded time integrals*, 33 page preprint, in preparation September 2014.
10. F. W. J. Olver, *Asymptotics and Special Functions* (Academic Press, New York and London, 1974).
11. F. W. J. Olver, *The Asymptotic Expansion of Bessel Functions of Large Order*, Phil. Trans. Roy. Soc. Lond. A 247 (1954) 328-368.
12. M. Abramowitz and I. A. Stegun, *Handbook of Mathematical Functions* (Dover Publishing Inc., New York, 1970).
13. G. N. Watson, *A Treatise on the Theory of Bessel Functions*, second edition (Cambridge University Press, Cambridge, 1944).
14. I. J. Thompson and A. R. Barnett, *Coulomb and Bessel functions of complex arguments and order*, J. Comp. Phys. 64, issue 2 (1986) 490-509.
15. S. E. Field, J. S. Hesthaven, and S. R. Lau, *Persistent junk solutions in time-domain modeling of extreme mass ratio binaries*, Phys. Rev. D81, 124030 (2010) [14 pages].
16. S. R. Lau, *Analytic structure of radiation boundary kernels for blackhole perturbations*, J. Math. Phys. 46 (2005) 102503 [21 pages].
17. S. R. Lau, *Rapid evaluation of radiation boundary kernels for time-domain wave propagation on blackholes: theory and numerical methods*, J. Comput. Phys. 199 (2004) 376-422.
18. Kernels are available at either of the following websites.
www.math.unm.edu/~lau/KernelsRWZ
www.dam.brown.edu/people/sfield/KernelsRWZ